MATERIALS CHEMISTRY FRONTIERS

RESEARCH ARTICLE

View Article Online
View Journal

Cite this: DOI: 10.1039/d6qm00032k

Strong confinement *via* 2D-to-3D zeolite transformation enables blue-emitting $CsPbBr_3$ quantum dots for backlight displays

Hongkai Li,[a] Yuchi Zhang,[a] Le Han,[a] Changshuai Gong[a] and Yan Xu *[ab]

Received 15th January 2026,
Accepted 2nd April 2026

DOI: 10.1039/d6qm00032k

rsc.li/frontiers-materials

Blue-emitting $CsPbBr_3$ perovskite quantum dots (PQDs) typically face challenges, such as low photoluminescence quantum yield (PLQY) and poor spectral stability, hindering their optoelectronic applications. Here, a feasible strategy was developed to encapsulate $CsPbBr_3$ PQDs within the supercages of a three-dimensional (3D) MCM-22 zeolite *via* structural transformation from its two-dimensional (2D) layered precursor (MCM-22P). CsBr and $PbBr_2$ were thoroughly mixed with high-surface-area MCM-22P nanosheets. Upon high-temperature treatment, MCM-22P condensed into a 3D framework with nanoscale interlayer spaces effectively suppressing $CsPbBr_3$ PQD aggregation, enabling uniform confinement of ultrafine $CsPbBr_3$ PQDs (2.13 nm) with stable blue emission at 467 nm and a maximum PLQY of 45.31%. A white-light-emitting diode (WLED) device with CIE color coordinates (0.31, 0.30) was constructed by combining $CsPbBr_3$@MCM-22-6h (blue), $CsPbBr_3$@MCM-22-0.5h (green), and KSF:Mn^{4+} phosphors (red) on a 365 nm chip. This work offers a very simple strategy for developing bright and deep-blue-emitting $CsPbBr_3$ PQDs for advanced optoelectronic applications.

Introduction

In solid-state lighting and display applications, commercial phosphors such as β-SiAlON:Eu^{2+} or $BaMgAl_{10}O_{17}$:Eu^{2+} typically exhibit high photoluminescence quantum yields (PLQY) and good stability, but still face certain limitations in spectral tunability.[1,2] In contrast, all-inorganic $CsPbX_3$ (X = Cl, Br, I) perovskite quantum dots (PQDs) have gained considerable attention for their outstanding optoelectronic properties, including high PLQY, tunable emission wavelengths, and excellent color purity.[3–6] These characteristics make $CsPbX_3$ PQDs promising for next-generation optoelectronic devices, such as light-emitting diodes (LEDs), backlight displays, photodetectors, and solar cells.[7–11] In recent years, various synthetic strategies have focused on developing green- and red-emitting PQDs with near-unity PLQY and excellent stability.[12,13] However, the synthesis of blue-emitting $CsPbX_3$ PQDs still faces significant challenges in achieving high efficiency and stability, primarily due to the uncontrollable phase fusion and difficulties in size regulation.[14] Thus, developing rational strategies to simultaneously optimize the bandgap structure and realize ultrastable blue emission in $CsPbX_3$ PQDs is urgently needed for advancing their optoelectronic applications.

To date, various approaches have been explored to achieve blue-emitting $CsPbX_3$ PQDs. The most widely used method involves adjusting the Cl^-/Br^- ratio in $CsPbCl_xBr_{3-x}$.[15] However, this approach is limited by halide ion migration and phase segregation, often resulting in red-shifted emission under optical or electrical excitation.[16,17] An alternative strategy involves reducing the dimensionality of $CsPbBr_3$ PQDs to form two-dimensional nanoplatelets (NPLs), in which enhanced quantum confinement effects facilitate blue emission.[18,19] Although $CsPbBr_3$ nanoplatelets can achieve relatively high PLQY in the blue region,[20] their environmental stability remains a challenge due to the high density of surface defects and large specific surface area.[21] Moreover, these nanoplatelets are typically present in colloidal form, which may hinder their direct integration into practical optoelectronic devices.[22] In this regard, cryogenic temperature synthesis, which features thermodynamically suppressed reaction kinetics, has demonstrated significant potential for precisely tailoring particle size and emission properties.[23] However, these approaches still encounter notable challenges, including poor size uniformity, emission instability, and limited control over nucleation and growth dynamics during the synthesis process.[24,25] To overcome these limitations, various approaches, including *in situ* ligand passivation, post-synthetic treatments, encapsulation, and A- and B-site doping, have been developed to enhance

[a] *Department of Chemistry, College of Sciences, Northeastern University, Shenyang, Liaoning 110819, P. R. China. E-mail: xuyan@mail.neu.edu.cn*
[b] *Foshan Graduate School of Innovation, Northeastern University, Foshan, Guangdong, 528311, P. R. China*

the photoluminescence efficiency and stability of $CsPbBr_3$ nanocrystals.[26,27] Nevertheless, achieving the simultaneous optimization of high efficiency and long-term stability in the blue emission region remains a significant challenge.

Recently, zeolites have emerged as effective hosts for the *in situ* growth and stabilization of $CsPbBr_3$ perovskite quantum dots (PQDs).[28,29] Their well-defined nanoscale cavities serve as templates that confine and isolate the growth of perovskite nanocrystals, thereby enabling uniform quantum confinement and enhancing structural stability. However, only a few studies have reported the fabrication of small-sized blue-emitting perovskite quantum dots using the confinement effect of zeolites. For instance, Yu *et al.* proposed a high-temperature evaporation method to incorporate $CsPbBr_3$ nanoparticles into the silicalite-1 zeolite doped with tungsten, achieving precise size tuning in the range of 2–6 nm, accompanied by tunable fluorescence emission from 468 to 508 nm.[28] Subsequent amino acid passivation and silane modification further suppressed the crystal aggregation even with soaking in aqueous solution and improved the photoluminescence efficiency with a highest PLQY of up to 76.93%. In our previous work, we encapsulated $CsPbBr_3$ PQDs within the nano-S-1 zeolite using a high-temperature solid-state method, resulting in blue-emitting quantum dots with an ultrasmall particle size of 2.38 nm, an emission wavelength of 474 nm, and a high PLQY of 44.4%.[29] Further hydrophobic treatment using octadecyltrimethoxysilane (ODTMS) ensured exceptional blue emission stability. Exploring simpler yet highly effective confinement strategies remains a significant challenge for realizing stable blue emission from $CsPbX_3$ PQDs for various optical applications.

Herein, we report a synergistic solid-state diffusion and thermally driven dimension-incremental strategy to achieve *in situ* nucleation and growth of blue-emitting $CsPbBr_3$ PQDs within the MCM-22 zeolite matrix. The $CsPbBr_3$ precursors are initially introduced into the interlayer spaces of a two-dimensional layered MCM-22P zeolite precursor, spaced by a hexamethyleneimine (HMI) organic template and interconnected through hydrogen bonding between silanol groups.[30] Upon high-temperature treatment, a 2D-to-3D structural transformation of the MCM-22P framework occurs accompanied by the removal of the template, forming well-defined interlayer twelve-membered ring (12 MR) supercages connected with double six-membered rings (6 MR). These supercages strongly confine ultrasmall $CsPbBr_3$ PQDs, preventing their aggregation and ensuring their uniform dispersion within the zeolite host.[31] By varying the calcination duration, we successfully reduced the nanoconfined size of $CsPbBr_3$ PQDs from 4.75 nm to 2.13 nm, achieving tunable photoluminescence spanning from green to deep blue (515–467 nm), with a maximum PLQY of 45.31% at sky-blue emission. Thus, the condensation of the layered MCM-22P matrix not only provides spatial confinement for uniform growth of ultrasmall $CsPbBr_3$ PQDs but also suppresses surface defect formation, thereby providing a perspective for the synthesis of an ultrastable blue-emitting perovskite composite for optical device applications.

Experimental

Chemicals

All chemicals were used as purchased without any further purification. The raw materials used in this research work include sodium metaaluminate ($NaAlO_2$, Macklin, AR, 99.5 wt%), colloidal silica (30 wt% suspension in water), sodium hydroxide (NaOH, Tianjin Damao, AR, 99 wt%), hexamethyleneimine (HMI, Aladdin, 98 wt%), cesium bromide (CsBr, Macklin, 99.5 wt%), lead(II) bromide (PbBr2, Aladdin, 99 wt%), and anhydrous ethanol (Tianjin Fuyu, AR, 99.5 wt%). All chemicals were used directly without further purification.

Syntheses of MCM-22P and MCM-22

The layered MCM-22 precursor (MCM-22P) was synthesized by employing a conventional hydrothermal method as previously described.[31] Firstly, $NaAlO_2$ and NaOH were dissolved in deionized water under vigorous stirring. Colloidal silica (30 wt% suspension in water) and hexamethyleneimine (HMI) were further added to the above mixture to obtain a homogeneous solution. The solution was then stirred continuously at room temperature for 3–4 h to guarantee complete homogeneity. The final gel was precisely controlled at a molar ratio of 50 SiO_2 : 1 Al_2O_3 : 2.5 Na_2O : 10 HMI : 580 H_2O. This gel was subsequently transferred into a Teflon-lined stainless steel autoclave and subjected to hydrothermal crystallization at 143 °C under rotation (60 rpm) for 4 days. After naturally cooling to room temperature, the solid product was isolated *via* vacuum filtration, thoroughly washed with distilled water until the filtrate pH dropped below 9, and finally dried under vacuum at 60 °C for 24 h. The synthesized product was denoted as MCM-22P.

To obtain the three-dimensional MCM-22 zeolite, the as-synthesized layered MCM-22P precursor was calcined in a flow of air at 550 °C for 6 h to completely remove the organic templates.

Synthesis of the $CsPbBr_3$@MCM-22 composite

In this part, stoichiometric amounts of CsBr and $PbBr_2$ (molar ratio = 1 : 1) were first mixed and ground with 90 mg of MCM-22P zeolite precursor to preliminarily homogenize the solid components. Subsequently, anhydrous ethanol was added to the pre-ground mixture, followed by further grinding for an additional 5 min. The introduction of ethanol during this second grinding stage significantly enhanced the uniform dispersion of reactants and minimized localized agglomeration or premature crystallization, facilitating the homogeneous formation of $CsPbBr_3$ PQDs in the subsequent calcination step. Following the complete evaporation of ethanol, the obtained homogeneous mixture was transferred into a quartz crucible and calcined at 550 °C for 6 h. After naturally cooling to room temperature, the resulting product was washed with deionized water for 20 min to remove residual $CsPbBr_3$ PQDs deposited on the zeolite surface and subsequently dried at ambient temperature. The final composite was designated as $CsPbBr_3$@MCM-22-6h.

Two shorter calcination times of 0.5 and 3 h were also applied for preparing the composites with all other experimental conditions kept constant. The final products were designated as $CsPbBr_3$@MCM-22-0.5h and $CsPbBr_3$@MCM-22-3h, respectively.

Characterization studies

X-ray diffraction (XRD) patterns of samples were measured on an X'Pert Pro MRDDY2094 diffractometer in the 2θ range of 2–10° and 5–40° using a Cu-Ka radiation (λ = 1.5418). The morphology was examined using an Ultra Plus field emission scanning electron microscope (FE-SEM, Hitachi SU8010). A JEOL JSM2100F microscope with a 200 kV accelerating voltage was used to perform the transmission electron microscope (TEM) and high-resolution transmission electron microscope (HRTEM) characterization studies. Scanning transmission electron microscopy (STEM) images were acquired using a Thermo Fisher Talos F200X G2 electron microscope, equipped with a Super-X energy dispersive spectroscopy (EDS) detector for surface chemical composition analysis. N_2 physical adsorption–desorption of the samples was measured using a fully automated specific surface and porosity analyzer (BET, ASAP2460). Thermogravimetric analysis (TGA) was performed using a TA Instruments TGA-50 analyzer by heating samples from room temperature to 800 °C at a rate of 10 °C min^{-1} under an oxygen atmosphere. Photoluminescence (PL) spectra were acquired using a fluorescence spectrophotometer (FluoroMax-4, HORIBA) and a 150 W xenon lamp was used as the excitation source. The luminescence decay curves were recorded using an Edinburgh Instruments FLS980 spectrometer. An X-ray photoelectron spectrometer (KRATOS, Ultra DLD, UK) was utilized to determine the chemical state of each element in the samples. A UV-Vis NIR spectrophotometer (Lambda 750 s, PerkinElmer, America) was used to evaluate the solid absorption UV spectra of different samples. The PLQY and the fluorescence lifetime were determined using a UV-vis near infrared fluorescence test system (Edinburgh, FLS1000). The photoelectric properties of white LED were measured using an auto-temperature LED photoelectric analyzer (ATA-1000, Everfine, China).

Results and discussion

As shown in Scheme 1, a two-dimensional zeolite precursor MCM-22P was first synthesized using a hydrothermal method. Subsequently, CsBr and $PbBr_2$ were introduced under a high-temperature solid-state diffusion condition to prepare the $CsPbBr_3$@MCM-22 composites. During this process, the perovskite precursors CsBr and $PbBr_2$ undergo reactions (1) and (2) upon grinding to form $CsPb_2Br_5$ and $CsPbBr_3$, and subsequent heating triggers reactions (3) and (4), which fully convert $CsPb_2Br_5$ into $CsPbBr_3$ (Fig. S1 in the SI).[28] Concurrently, the lamellar MCM-22P precursor gradually transforms into a three-dimensional MCM-22 zeolite upon template removal, with adjacent layers condensing to form interlayer 12-membered-ring (12-MR) supercages. Within these cavities, ultrasmall and highly stable $CsPbBr_3$ PQDs nucleated and were spatially confined *in situ* through thermal treatment followed by water washing.

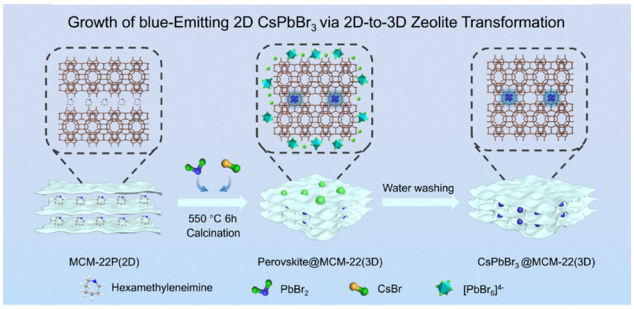

Scheme 1 Schematic illustration of the synthetic procedure of the $CsPbBr_3$@MCM-22 composite.

As shown in Fig. S2 in the SI, the XRD patterns of MCM-22P and calcined MCM-22 exhibit high crystallinity and phase purity. All diffraction peaks are consistent in position with those reported in the literature for MWW-type zeolites.[31–33] For MCM-22P, the prominent (002) reflection at 2θ = 6.5° corresponds to interlayer stacking along the *c*-axis.[32] Additional reflections at 2θ = 7.1°, 24.9°, and 26.0° are indexed to the (101), (220), and (310) planes, respectively. After calcination, the attenuation of the (002) peak and its overlap with the emerging (100) reflection confirm the condensation of silanol groups and the formation of a three-dimensional MCM-22 framework.[34] SEM images in Fig. S3 in the SI show that both MCM-22P and calcined MCM-22 retain thin plate-like morphology. The preservation of the external structure indicates that internal condensation has a minimal effect on the macroscopic shape of the zeolite crystals.

The XRD pattern of the $CsPbBr_3$@MCM-22 composite, obtained after encapsulating $CsPbBr_3$ PQDs *via* thermal-driven expansion of MCM-22P, closely resembles that of the three-dimensional MWW-type structure of the MCM-22 framework (Fig. S4a in the SI). This indicates that the *in situ* nucleation and growth of $CsPbBr_3$ has little effect on the 2D-to-3D structural transformation of the MCM-22P precursor into the MCM-22 zeolite framework. Moreover, the diffraction peaks of $CsPbBr_3$ PQDs were undetectable in the synthesized composites compared to the XRD standard card (PDF#54-0752) of $CsPbBr_3$, likely due to the low content of confined $CsPbBr_3$ PQDs within the interlayer 12-MR supercages after a six hour calcination at 550 °C. SEM and TEM images (Fig. S4b in the SI and Fig. 1a) demonstrate that the morphology of MCM-22 platelets is also well preserved after $CsPbBr_3$ PQD incorporation. The STEM image (Fig. 1b) shows the uniform dispersion of $CsPbBr_3$ PQDs, while the HRTEM image (Fig. 1c) reveals a lattice spacing of 0.29 nm, corresponding to the (200) crystal plane of $CsPbBr_3$. The well-aligned diffraction spots obtained FFT in the inset of Fig. 1c further indicate the single-crystal structure of $CsPbBr_3$ PQDs.[24] HRTEM images and fast Fourier transform (FFT) analysis (Fig. 1d–f) confirm that the hexagonal structure of MCM-22 remains unchanged after the incorporation

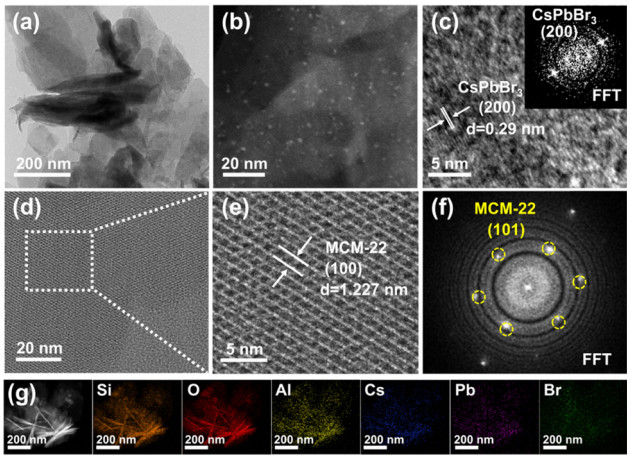

Fig. 1 (a) TEM image of $CsPbBr_3$@MCM-22 composite. (b) STEM images and (c)–(f) HRTEM images with corresponding FFT patterns of the $CsPbBr_3$@MCM-22 composite. (g) EDS mapping images of Si, O, Al, Cs, Pb and Br elements in the composite.

of $CsPbBr_3$ PQDs, with a measured lattice spacing of 1.227 nm corresponding to the MWW (100) plane,[35,36] consistent with the XRD observations. EDS elemental mapping (Fig. 1g) reveal a homogeneous distribution of Cs, Pb, and Br within the zeolite framework, confirming the successful and uniform incorporation of $CsPbBr_3$ PQDs.

Nitrogen adsorption–desorption isotherms of MCM-22 and $CsPbBr_3$@MCM-22 samples and the corresponding pore size distribution curves are shown in Fig. 2. The isotherms of both pristine MCM-22 and $CsPbBr_3$@MCM-22 composites can be classified as a combination of Type I and Type IV according to the International Union of Pure and Applied Chemistry (IUPAC) classification (Fig. 2a). All samples exhibit a pronounced increase in N_2 adsorption at low relative pressures ($P/P_0 < 0.1$), which is a characteristic feature of microporous materials. At higher P/P_0 values, a distinct hysteresis loop is observed, which can be attributed to the accumulation of crystal nanosheets, resulting in the formation of interparticle mesopores (Fig. 2b).[36] Upon the incorporation of $CsPbBr_3$ PQDs, the total nitrogen uptake decreased significantly, and the BET surface area dropped from 415 $m^2\ g^{-1}$ to 73 $m^2\ g^{-1}$ (Table S1 in the SI), indicating partial pore filling and volume occupation by the embedded $CsPbBr_3$ nanocrystals. Moreover, a pronounced decrease in the pore population of the zeolite was

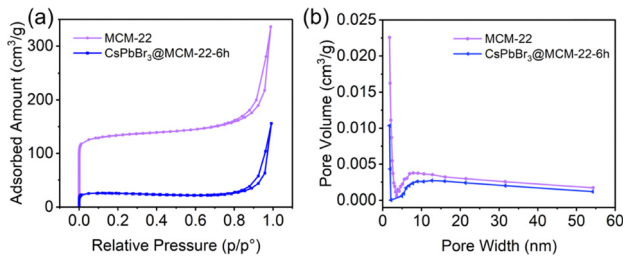

Fig. 2 (a) N_2 adsorption–desorption isotherm and the corresponding (b) DJH pore size distribution of MCM-22 and $CsPbBr_3$@MCM-22-6h.

observed, further confirming the successful encapsulation of $CsPbBr_3$ PQDs within the MCM-22 framework.

To optimize the thermally driven dimension-incremental process for controlling the nucleation and growth of blue-emitting $CsPbBr_3$ PQDs, we conducted TGA analysis of the MCM-22P host matrix at various calcination durations to evaluate the template removal efficiency and structural stability, and the results are shown in Fig. S5 and Table S2 in the SI. For MCM-22P-0.5h, the weight loss occurred in three stages: stage 1 (50–150 °C) is due to the removal of physisorbed water; stage 2 (150–400 °C) results from the decomposition of HMI templates in the interlayer regions; and stage 3 (>400 °C) is caused by the decomposition of HMI bound in the 10-MR channels (Fig. S5 and Table S2 in the SI).[37] In contrast, the MCM-22P-6h exhibits little mass loss at high temperature, indicating a complete removal of interlayer HMI and a full transformation from the layered MCM-22P precursor to the three-dimensional MWW structure. Accordingly, a series of $CsPbBr_3$@MCM-22-x composites (x = 0.5, 3, and 6 h) were synthesized by varying calcination durations to study how the structural evolution affects the growth of $CsPbBr_3$ PQDs. As the calcination time increased from 0.5 to 6 h, the average size of $CsPbBr_3$ PQDs within the zeolite progressively decreased from 4.75 nm to 2.13 nm (Fig. 3a–f). This size evolution reveals a critical dependence of the $CsPbBr_3$ PQD growth behavior on the removal efficiency of HMI templates. At the initial calcination stage, residual HMI impedes the complete formation of interlayer supercages and restricts the diffusion of $CsPbBr_3$ precursors into the interlayer space. Consequently, the $CsPbBr_3$ precursors preferentially nucleate at the framework interruptions, forming larger $CsPbBr_3$ PQDs with poor thermal stability that gradually detach from the zeolite host under prolonged heating. With complete removal of HMI, the structural condensation of the zeolite framework is promoted, yielding well-developed supercages with 12-MR windows. These nanocavities function as ideal nanoreactors, strongly confining nucleation and growth of ultrasmall $CsPbBr_3$ PQDs, thereby reducing the overall particle size of $CsPbBr_3$ PQDs and improving size uniformity (Fig. 3g). Furthermore, this confinement strategy can be extended to other halide perovskites, evidenced by blue shifts in the emission peaks of $CsPbI_3$ and $CsPbCl_3$ as the calcination time increased from 0.5 h to 6 h (Fig. S6 in the SI), confirming its broad applicability across halide compositions and tunability of emission properties.

The optical properties of different size-distributed $CsPbBr_3$ PQDs confined in MCM-22 zeolite nanosheets were investigated. Fig. 4a shows the solid-state UV absorption and PL spectra of $CsPbBr_3$@MCM-22-x composites (x = 0.5 h, 3 h, and 6 h) prepared with varying calcination times. When the calcination time increases from 0.5 h to 6 h, the emission peak of the composites blue-shifts from 515 nm to 467 nm, and the corresponding excitation absorption peak also exhibits a significant blue-shift. Meanwhile, the color changes distinctly from green to deep blue under 365 nm UV light (Fig. S7 in SI), and the corresponding CIE diagrams are shown in Fig. S8 in SI. Tauc plot analysis (Fig. 4b) reveals a gradual increase in

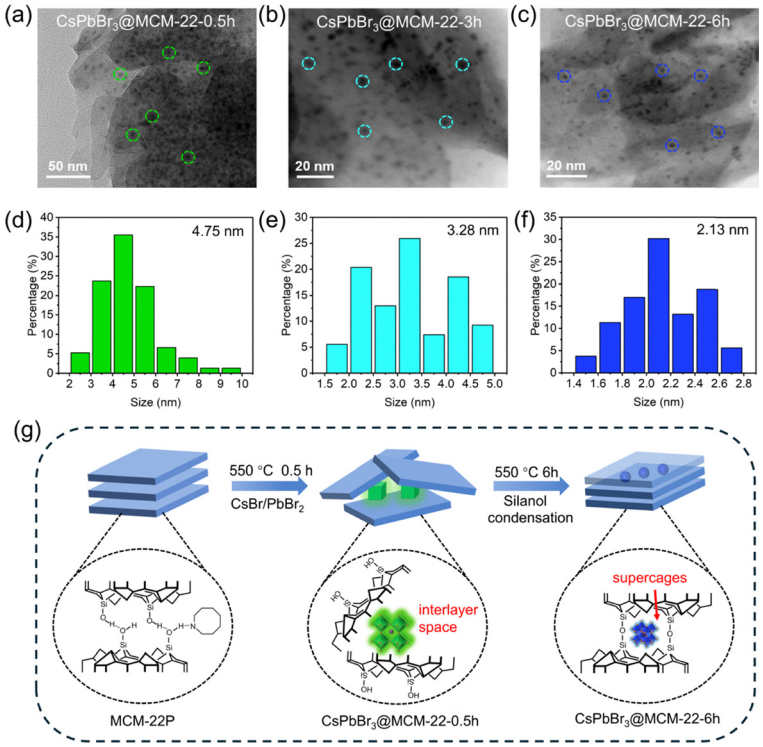

Fig. 3 Morphology properties of $CsPbBr_3$@MCM-22 composites obtained in different conditions. (a)–(c) TEM images of various sized $CsPbBr_3$ PQDs confined in the MCM-22 matrix. (d)–(f) Corresponding size distribution. (g) Influence of calcination duration on the controlled confinement of $CsPbBr_3$ PQDs with different particle sizes.

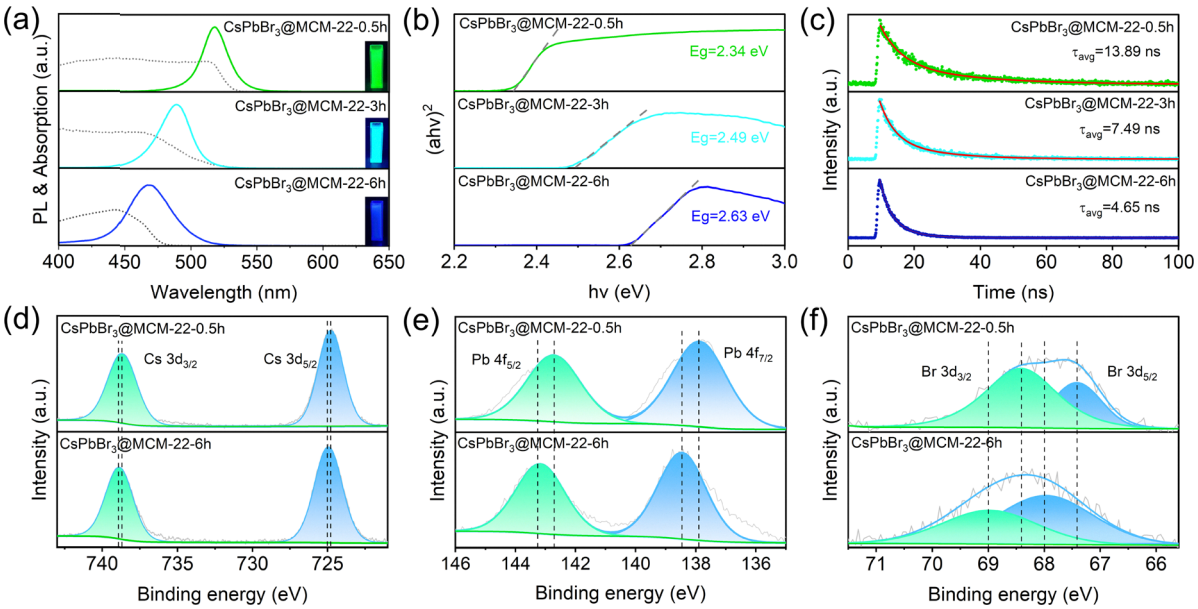

Fig. 4 Optical properties of the $CsPbBr_3$@MCM-22 composites. (a) Solid-state UV absorption and PL spectra, (b) Tauc-plot curves, and (c) time-resolved PL decay curves. (d)–(f) Comparison of XPS spectra of $CsPbBr_3$@MCM-22-0.5h and $CsPbBr_3$@MCM-22-6h.

optical bandgap from 2.34 eV to 2.63 eV, providing direct evidence that the band structure broadens with decreasing $CsPbBr_3$ PQD size, consistent with quantum confinement effects.[28] In addition, the fluorescence lifetimes decrease from 13.89 ns to 4.65 ns (Fig. 4c), and the corresponding PLQYs are 44.21%, 45.31%, and 19.34% for $CsPbBr_3$@MCM-22-0.5h, $CsPbBr_3$@MCM-22-3h, and $CsPbBr_3$@MCM-22-6h, respectively (Fig. S9 in the SI). The relatively low PLQY of the

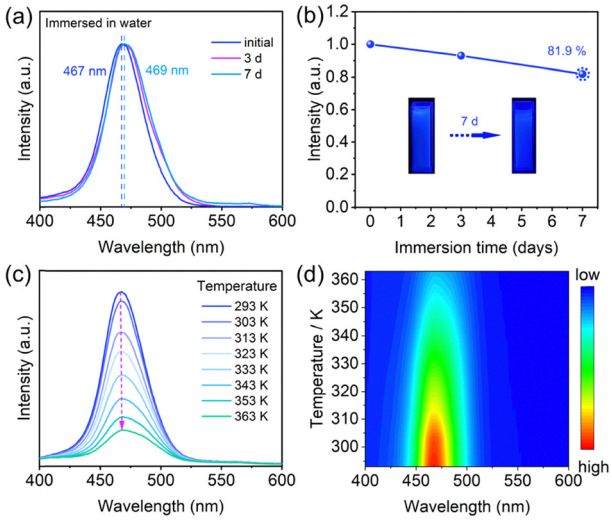

Fig. 5 (a) Normalized PL intensity test and (b) PL intensity of $CsPbBr_3$@MCM-22-6h suspended in water for 7 days. (c) Corresponding temperature-dependent PL spectra (λ_{ex} = 365 nm) and (d) 2D contour plots.

deep-blue-emitting $CsPbBr_3$@MCM-22-6h mainly stems from enhanced quantum confinement effects. Smaller nanocrystals exhibit a much higher surface-to-volume ratio, which strengthens surface interactions and accelerates nonradiative recombination.[38]

The XPS spectra of selected $CsPbBr_3$@MCM-22-0.5h and $CsPbBr_3$@MCM-22-6h samples were also measured to investigate the influence of spatial confinement on the formation of $CsPbBr_3$ PQDs. As shown in Fig. S10 in the SI, after charge correction using the characteristic C 1s peak at 284.8 eV, their survey spectra reveal the presence of oxygen (O), silicon (Si), cesium (Cs), lead (Pb), and bromine (Br) elements. Compared with green-emitting $CsPbBr_3$@MCM-22-0.5h, the blue-emitting $CsPbBr_3$@MCM-22-6h exhibits a distinct positive shift in the Cs 3d, Pb 4f, and Br 3d XPS peaks toward higher binding energies (Fig. 4d–f), providing evidence for the lattice contraction of $CsPbBr_3$ nanocrystals in $CsPbBr_3$@MCM-22-6h, which is consistent with the observed reduction in particle size and the blue-shifted emission.[24,29]

The stability of $CsPbBr_3$ composites is crucial for practical applications. Unlike bare $CsPbBr_3$ nanocrystals, which undergo fluorescence quenching due to decomposition into Cs^+ and $[PbX_6]^{4-}$ upon exposure to moisture and water,[28,39,40] the $CsPbBr_3$@MCM-22-6h retained bright blue emission with negligible intensity loss after one month of storage under ambient conditions (Fig. S11 in the SI), confirming its excellent long-term stability. Moreover, the emission intensity remains nearly unchanged after continuous irradiation under a 365 nm UV lamp for 48 h (Fig. S12 in the SI), demonstrating its outstanding photostability. After ultrasonic dispersion in deionized water for 7 days, $CsPbBr_3$@MCM-22-6h exhibited only a minor red-shift of ≈2 nm in its emission peak (Fig. 5a), and the PL intensity remained at 81.9% of the initial value (Fig. 5b), demonstrating remarkable water stability. Furthermore, thermal stability was assessed by recording temperature-dependent

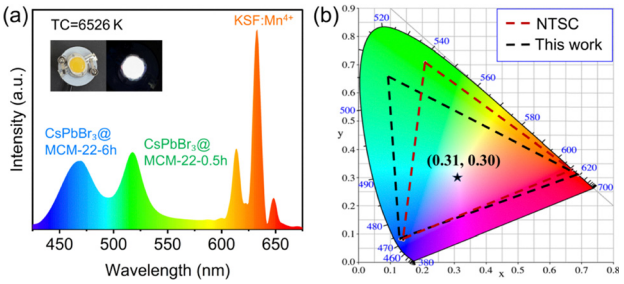

Fig. 6 (a) The spectra and (b) corresponding color coordinates of the WLED device.

PL spectra of $CsPbBr_3$@MCM-22-6h from 20 °C to 90 °C (Fig. 5c) and constructing a two-dimensional emission contour plot (Fig. 5d). Although the PL intensity slightly decreased with increasing temperature due to enhanced nonradiative processes, the emission peak remained fixed in the blue region, indicating that the particle size of $CsPbBr_3$ PQDs was well preserved after exposure to elevated temperatures. Overall, the prepared $CsPbBr_3$@MCM-22 composite exhibits superior resistance to moisture and heat compared to previously reported blue-emitting $CsPbBr_3$ PQDs (Table S3 in the SI). The exceptional stability stems from the strong spatial confinement of *in situ* formed interlayer supercages generated by 2D-to-3D transformation of the MCM-22 zeolite, enabling high resistance to ion migration, aggregation, and structural degradation under harsh conditions.[35]

A white light-emitting diode (WLED) was constructed by integrating $CsPbBr_3$@MCM-22 composites with commercial $KSF:Mn^{4+}$ phosphor onto a 365 nm UV LED chip (Fig. 6). $CsPbBr_3$@MCM-22-0.5h (green emission), $CsPbBr_3$@MCM-22-6h (blue emission), and $KSF:Mn^{4+}$ (red emission) formed a standard tricolor configuration for white-light (Fig. 6a), indicating efficient color mixing of the components. Consequently, the packaged device emitted bright cool white light with a correlated color temperature (CCT) of 6526 K, as shown in the illumination photographs taken under 20 mA (inset of Fig. 6a). The PL spectrum covered nearly the entire visible region, corresponding to 104.3% of the NTSC color space, and a cool white light with CIE color coordinates of (0.31, 0.30) was achieved by adjusting the relative proportions of the components (Fig. 6b).

Conclusions

In conclusion, this work demonstrates the controllable growth of blue-emitting $CsPbBr_3$ perovskite quantum dots (PQDs) within the MCM-22 zeolite through a 2D-to-3D zeolite transformation strategy. This process creates abundant interconnected supercages that provide a strong confinement effect for the uniform growth of ultrasmall $CsPbBr_3$ nanocrystals. As the calcination duration increases, the average particle size of $CsPbBr_3$ PQDs decreases from 4.75 nm to 2.13 nm, accompanied by a photoluminescence blue shift from 515 nm (green) to 467 nm (deep blue) and a maximum PLQY of 45.31% at sky-blue emission. Moreover, the condensed nanopores stem from

2D-to-3D structural transformation of MCM-22 effectively suppresses the migration and aggregation of $CsPbBr_3$ PQDs, endowing it excellent blue emission stability. Subsequently, a white light-emitting diode (WLED) was developed for backlight display applications by combining blue-emitting $CsPbBr_3$@MCM-22 with a commercial KSF:Mn^{4+} phosphor. This work presents a simple thermal-driven 2D-to-3D zeolite transformation strategy to afford the growth of ultrasmall and highly stable blue-emitting $CsPbBr_3$ PQDs within the MCM-22 zeolite, offering new insights and pathways for high-performance perovskite light-emitting devices. Future work will focus on further improving the PLQY of deep-blue $CsPbBr_3$ PQD emitters by integrating this approach with surface passivation strategies.

Conflicts of interest

There are no conflicts to declare.

Data availability

Data are available upon request from the authors.

Supplementary information (SI), including XRD, SEM, TG, PL spectra, photoluminescence lifetime data, XPS, BET surface area comparisons of samples, and luminescence performance comparisons with related reported materials. See DOI: **https://doi.org/10.1039/d6qm00032k**.

Acknowledgements

The present work was supported by the Guangdong Basic and Applied Basic Research Foundation (No. 2023A1515140011), the National Natural Science Foundation of China (Grant No. 22171040), and the Shenyang Young and Middle-aged Science and Technology Innovation Talent Support Program (No. RC230784).

References

1 X. Y. Zhang, W. Y. Li, C. Wang, L. Zhang, S. X. Li and R.-J. Xie, Narrow-Band Green Nitride Phosphor for Wide Color Gamut Backlighting, *Chem. Eng. J.*, 2025, **509**, 161073.

2 S. Jeet and O. P. Pandey, Template free synthesis route to monophasic $BaMgAl_{10}O_{17}:Eu^{2+}$ with high luminescence efficiency, *J. Alloys Compd.*, 2018, **750**, 85–91.

3 L. Protesescu, S. Yakunin, M. I. Bodnarchuk, F. Krieg, R. Caputo, C. H. Hendon, R. X. Yang, A. Walsh and M. V. Kovalenko, Nanocrystals of cesium lead halide perovskites ($CsPbX_3$, X = Cl, Br, and I): novel optoelectronic materials showing bright emission with wide color gamut, *Nano Lett.*, 2015, **15**, 3692–3696.

4 D. Q. Chen, Y. Liu, C. B. Yang, J. S. Zhong, S. Zhou, J. K. Chen and H. Huang, Promoting photoluminescence quantum yields of glass-stabilized $CsPbX_3$ (X = Cl, Br, I) perovskite quantum dots through fluorine doping, *Nanoscale*, 2019, **11**, 17216–17221.

5 A. N. Singh, S. Kajal, J. Kim, A. Jana, J. Y. Kim and K. S. Kim, Interface Engineering Driven Stabilization of Halide Perovskites against Moisture, Heat, and Light for Optoelectronic Applications, *Adv. Energy Mater.*, 2020, **10**, 2000768.

6 X. W. Yu, K. K. Liu, B. L. Wang, H. Y. Zhang, Y. Y. Qi and J. H. Yu, Time-Dependent Polychrome Stereoscopic Luminescence Triggered by Resonance Energy Transfer Between Carbon Dots-in-Zeolite Composites and Fluorescence Quantum Dots, *Adv. Mater.*, 2023, **35**, 2208735.

7 X. G. Wu, H. L. Ji, X. L. Yan and H. Z. Zhong, Industry outlook of perovskite quantum dots for display applications, *Nat. Nanotechnol.*, 2022, **17**, 813–816.

8 W. G. Chi and S. K. Banerjee, Application of Perovskite Quantum Dots as an Absorber in Perovskite Solar Cells, *Angew. Chem., Int. Ed.*, 2022, **61**, 202112412–202112431.

9 Y. Liu, Y. T. Dong, T. Zhu, D. X. Ma, A. Proppe, B. Chen, C. Zheng, Y. Hou, S. Lee, B. Sun, E. H. Jung, F. L. Yuan, Y. K. Wang, L. K. Sagar, S. Hoogland, F. P. G. Arquer, M. J. Choi, K. Singh, S. O. Kelley, O. Voznyy, Z. H. Lu and E. H. Sargent, Bright and Stable Light-Emitting Diodes Based on Perovskite Quantum Dots in Perovskite Matrix, *J. Am. Chem. Soc.*, 2021, **143**, 15606–15615.

10 H. Zhou, Z. Song, C. R. Grice, C. Chen, J. Zhang, Y. F. Zhu, R. H. Liu, H. Wang and Y. F. Yan, Self-powered $CsPbBr_3$ nanowire photodetector with a vertical structure, *Nano Energy*, 2018, **53**, 880–886.

11 S. X. Chen, J. D. Lin, S. Zheng, Y. H. Zheng and D. Q. Chen, Efficient and Stable Perovskite White Light-Emitting Diodes for Backlit Display, *Adv. Funct. Mater.*, 2023, **33**, 2213442.

12 J. Y. Yin, F. Wu, J. N. Dai and C. Q. Chen, $CsPbBr_3$@$PbSO_4$ nanocomposites with near-unity photoluminescence and ultrastability via in-water in situ embedding synthesis strategy, *Chem. Eng. J.*, 2024, **499**, 156066.

13 J. Pan, Y. Q. Shang, J. Yin, M. D. Bastiani, W. Peng, I. Dursun, L. Sinatra, A. M. El-Zohry, M. N. Hedhili, A. H. Emwas, O. F. Mohammed, Z. J. Ning and O. M. Bakr, Bidentate ligand-passivated $CsPbI_3$ perovskite nanocrystals for stable near-unity photoluminescence quantum yeld and efficient red light-emitting diodes, *J. Am. Chem. Soc.*, 2018, **140**, 562–565.

14 X. Y. Qian, Y. Y. Tang, W. Zhou, Y. Shen, M. L. Guo, Y. Q. Li and J. X. Tang, Strategies to Improve Luminescence Efficiency and Stability of Blue Perovskite Light-Emitting Devices, *Small Sci.*, 2021, **1**, 2000048.

15 Y. J. Yoon, Y. S. Shin, H. Jang, J. G. Son, J. W. Kim, C. B. Park, D. Yuk, J. Seo, G. H. Kim and J. Y. Kim, Highly stable bulk perovskite for blue LEDs with anion-exchange method, *Nano Lett.*, 2021, **21**, 3473–3479.

16 I. L. Braly, R. J. Stoddard, A. Rajagopal, A. R. Uhl, J. K. Katahara, A. K. Y. Jen and H. W. Hillhouse, Current-induced phase segregation in mixed halide hybrid perovskites and its impact on two-terminal tandem solar cell design, *ACS Energy Lett.*, 2017, **2**, 1841–1847.

17 A. Haque, T. D. Chonamada, A. B. Dey and P. K. Santra, Insights into the Interparticle Mixing of $CsPbBr_3$ and $CsPbI_3$

nanocubes: Halide Ion Migration and Kinetics, *Nanoscale*, 2020, **12**, 20840–20848.

18 S. Kumar, J. Jagielski, S. Yakunin, P. Rice, Y. C. Chiu, M. C. Wang, G. Nedelcu, Y. Kim, S. C. Lin, E. J. G. Santos, M. V. Kovalenko and C. J. Shih, Efficient blue electroluminescence using quantum-confined two-dimensional perovskites, *ACS Nano*, 2016, **10**, 9720–9729.

19 Q. Y. Zhang, F. Y. Diao, X. Y. Xue, X. L. Sheng, D. Barba and Y. Q. Wang, Self-assembly of $CsPbBr_3$ nanocubes into 2D nanosheets, *ACS Appl. Mater. Interfaces*, 2021, **13**, 44777–44785.

20 S. R. Pathipati, M. N. Shah, S. Akhil and N. Mishra, In situ synthesis of high-quantum-efficiency and stable bromide-based blue-emitting perovskite nanoplatelets, *Nanoscale Adv.*, 2022, **4**, 4766–4781.

21 H. Lin, Q. Wei, K. W. Ng, J. Y. Dong, J. L. Li, W. W. Liu, S. S. Yan, S. Chen, G. C. Xing, X. S. Tang, Z. K. Tang and S. P. Wang, Stable and efficient blue-emitting $CsPbBr_3$ nanoplatelets with potassium bromide surface passivation, *Small*, 2021, **17**, 2101359.

22 X. Xiao, Y. Li and R.-J. Xie, Blue-emitting and self-assembled thinner perovskite $CsPbBr_3$ nanoplates: synthesis and formation mechanism, *Nanoscale*, 2020, **12**, 9231–9239.

23 J. J. Cao, C. Yan, C. Luo, W. Li, X. K. Zeng, Z. Xu, X. H. Fu, Q. Wang, X. Chu, H. C. Huang, X. Y. Zhao, J. Lu and W. Q. Yang, Cryogenic Temperature Thermodynamically Suppressed and Strongly Confined $CsPbBr_3$ Quantum Dots for Deeply Blue Light-Emitting Diodes, *Adv. Opt. Mater.*, 2021, **9**, 2100300.

24 Y. T. Dong, T. Qiao, D. Kim, D. Parobek, D. Rossi and D. H. Son, Precise Control of Quantum Confinement in Cesium Lead Halide Perovskite Quantum Dots via Thermodynamic Equilibrium, *Nano Lett.*, 2018, **18**, 3716–3722.

25 S. Singh, X. B. Tang and F. Q. Yang, Low-Temperature Synthesis of Highly Stable Blue-Emitting Perovskite $CsPbBr_3$ Quantum Dots, *J. Phys. Chem. C*, 2025, **129**, 3942–3950.

26 S. Chatterjee, S. Biswas, S. Sourav, J. Rath, S. Akhil and N. Mishra, Strategies To Achieve Long-Term Stability in Lead Halide Perovskite Nanocrystals and Its Optoelectronic Applications, *J. Phys. Chem. Lett.*, 2024, **15**, 10118–10137.

27 V. G. V. Dutt, S. Akhil and N. Mishra, Surface Passivation Strategies for Improving Photoluminescence and Stability of Cesium Lead Halide Perovskite Nanocrystals, *ChemNanoMat*, 2020, **6**, 1730–1742.

28 H. Y. Zhang, B. L. Wang, Z. J. Niu, G. R. Chen, B. Y. Guan, J. Y. Li and J. H. Yu, Ultrasmall water-stable $CsPbBr_3$ quantum dots with high intensity blue emission enabled by zeolite confinement engineering, *Mater. Horiz.*, 2023, **10**, 5079–5086.

29 Y. C. Zhang, H. K. Li, L. Han and Y. Xu, Engineering Green- to Blue-Emitting $CsPbBr_3$ Quantum Dots in Nanozeolite with High Stability for Backlight Display Application, *Nano Lett.*, 2024, **24**, 16400–16407.

30 Y. Wang, R. S. Peng, W. H. Sun, S. Q. Li, S. T. Wu, H. Xu, J. G. Jiang, S. F. Chen and P. Wu, Designable synthesis of layered silicates and tunable interlayer expanded to zeolites, *Small*, 2024, **20**, 2307323.

31 S. Molitorisová, Y. Y. Zhang, M. Kubů, A. Li, Z. Tošner and M. Shamzhy, 2D-to-3D zeolite transformation for the preparation of Pd@MWW catalysts with tuneable acidity, *Catal. Today*, 2022, **390**, 109–116.

32 Y. Y. Zhang, M. Kubů, M. Mazur and J. Čejka, Synthesis of Pt-MWW with controllable nanoparticle size, *Catal. Today*, 2019, **324**, 135–143.

33 P. Chatterjee, Y. Han, T. Kobayashi, K. K. Verma, M. Mais, R. K. Behera, T. H. Johnson, T. Prozorov, J. W. Evans, I. I. Slowing and W. Y. Huang, Capturing Rare-Earth Elements by Synthetic Aluminosilicate MCM-22: Mechanistic Understanding of Yb(III) Capture, *ACS Appl. Mater. Interfaces*, 2023, **15**, 54192–54201.

34 A. J. Schwanke, U. Díaz, A. Corma and S. Pergher, Recyclable swelling solutions for friendly preparation of pillared MWW-type zeolites, *Microporous Mesoporous Mater.*, 2017, **253**, 91–95.

35 L. Liu, U. Díaz, R. Arenal, G. Agostini, P. Concepción and A. Corma, Generation ofsubnanometric platinum with high stability during transformation of a 2D zeolite into 3D, *Nat. Mater.*, 2017, **16**, 132–138.

36 H. B. Li, C. N. Zhang, Q. Lin, F. Lin, T. S. Xiao, K. X. Yan, B. Shen, H. B. Zhang, Y. Tang and Z. Z. Sun, Epitaxial Growth of Two-Dimensional MWW Zeolite, *J. Am. Chem. Soc.*, 2024, **146**, 8520–8527.

37 X. Zhang, Y. Q. Wang, L. Z. Bu, X. M. Su, Y. N. Li, J. C. Sang, G. M. Ren and M. H. Wen, Precursor-seed-assisted facile synthesis of binder-free MCM-22 zeolite, *J. Porous Mater.*, 2025, **32**, 1763–1775.

38 G. Rainò, N. Yazdani, S. C. Boehme, M. Kober-Czerny, C. Zhu, F. Krieg, M. D. Rossell, R. Erni, V. Wood, I. Infante and M. V. Kovalenko, Ultra-narrow room-temperature emission from single $CsPbBr_3$ perovskite quantum dots, *Nat. Commun.*, 2022, **13**, 2587.

39 L. Han, B. H. Li, Y. C. Zhang and Y. Xu, Ultrastable emissive perovskite nanocomposite via dual protection of polymer grafted TS-1 zeolite for backlight display application, *Chem. Eng. J.*, 2023, **473**, 145323–145333.

40 Q. Xiong, S. H. Huang, J. Du, X. S. Tang, F. J. Zeng, Z. Z. Liu, Z. Y. Zhang, T. C. Shi, J. Yang, D. F. Wu, H. Lin, Z. T. Luo and Y. X. Leng, Surface ligand engineering for $CsPbBr_3$ quantum dots aiming at aggregation suppression and amplified spontaneous emission improvement, *Adv. Opt. Mater.*, 2020, **8**, 2000977.

